Materials Characterization 178 (2021) 111242

Contents lists available at ScienceDirect

Materials Characterization

journal homepage: www.elsevier.com/locate/matchar

Simultaneously minimizing residual stress and enhancing strength of selective laser melted nano-TiB_2 decorated Al alloy via post-uphill quenching and ageing

Y.K. Xiao [a], Z.Y. Bian [a], Y. Wu [b,*], G. Ji [c], Q. Lian [b], H.Z. Wang [b], Z. Chen [a,*], H.W. Wang [a]

[a] State Key Laboratory of Metal Matrix Composites, Shanghai Jiao Tong University, No. 800 Dongchuan Road, Shanghai 200240, China
[b] School of Materials Science & Engineering, Shanghai Jiao Tong University, No. 800 Dongchuan Road, Shanghai 200240, China
[c] Univ. Lille, CNRS, INRA, ENSCL, UMR 8207 - UMET - Unité Matériaux et Transformations, F-59000 Lille, France

ARTICLE INFO

Keywords:
Selective laser melting
Aluminium alloys
Uphill quenching and ageing
Residual stress
Mechanical properties

ABSTRACT

Selective laser melting (SLM) of aluminium alloys is of research interest to produce customized or complex-shaped metal components for functional or structural applications. In order to palliate the undesirable residual stress developed in the SLM process, traditional post-annealing heat treatment has been widely used to lower residual stress in selective laser melted (SLMed) Al alloys. However, the traditional post-annealing method usually leads to a decrease in strength which is another concern for applications. In this study, we developed and validated a new strategy combining post-uphill quenching and subsequent ageing to simultaneously minimise residual stress and increase the strength of SLMed nano-TiB_2 decorated Al alloy parts. The results show that the high as-built residual stress was partly counteracted by the newly-produced residual stress in the opposite direction during the uphill quenching stage and synergistically reduced by dislocation recovery during the ageing stage. The microstructural features of grains and cell structures remain unchanged after the treatment. While substantial new nano-Si particles with dot-like or needle-like morphology precipitate inside the cells. The tensile strength was improved mainly due to effective precipitation strengthening by dispersed nanosized Si precipitates. The proposed strategy is expected to be useful in other materials and components fabricated by SLM in which residual stress is also unwanted.

1. Introduction

Selective laser melting (SLM), as an emerging additive manufacturing (AM) technology for metals, alloys, and composites, has shown enormous potential in the aerospace, automobile, and medical industries, which demand complex geometries and individualised production [1,2]. The SLM process has been developed to produce high-quality parts with excellent mechanical properties [3,4]. However, one significant problem that must be solved urgently is the undesirable residual stress developed in the as-built state due to the unique thermal conditions (i.e., violent heating and cooling cycles inducing steep thermal gradients) [5–7].

Residual stress can be found in almost all SLMed alloys, including aluminium [8,9], superalloy [10,11], titanium [12,13], and stainless steel [14,15]. The presence of residual stress leads to significant design errors, makes processability difficult, and can even cause severe geometry distortions and cracks [6]. Thus, residual stress is a critical obstacle to the full-scale adoption of the SLM process in industrial applications. Owing to the above detrimental effects, residual stress and distortions in as-built parts must be reduced within a low range acceptable for applications. Al—Si series alloys, especially the hypoeutectic and eutectic Al—Si alloys, are the most commonly studied low-cost and attractive choices of Al alloys for weight-saving SLM applications. To date, a vast number of studies on SLMed Al—Si samples have reported the existence, magnitude, and distribution of residual stress [16–18] and its formation mechanism [14] to find practical solutions to residual stress reduction. For example, adjusting the scanning strategy can reduce residual stress to a certain extent, but the remaining residual stress is still high [14]. Pre-heating the base substrate, changing process parameters, post-solution heat treatment [19–23], and post-annealing [22–27] could also lower residual stress, but they also lead to strength loss, which is another concern for applications. To date, no

* Corresponding authors.
E-mail addresses: eagle51@sjtu.edu.cn (Y. Wu), zhe.chen@sjtu.edu.cn (Z. Chen).

https://doi.org/10.1016/j.matchar.2021.111242
Received 22 February 2021; Received in revised form 11 May 2021; Accepted 31 May 2021
Available online 1 June 2021

Table 1
Chemical compositions of TiB_2/Al-7Si-Mg alloy determined by ICP-AES (wt%).

Element	Si	Mg	Fe	Ti	B	Al
Powder	6.876	0.642	0.048	1.768	0.719	Balance
SLMed sample	6.801	0.628	0.051	1.751	0.718	Balance

effective approach to relieving the high residual stress in SLMed Al—Si series alloys without sacrificing strength has been presented.

Therefore, we propose a new approach combining post-uphill quenching and ageing (hereafter referred to as 'U + A') to relieve residual stress while simultaneously promoting precipitation strengthening in as-built parts. This U + A process reduces residual stress by introducing a new reverse residual stress (i.e., in the opposite direction

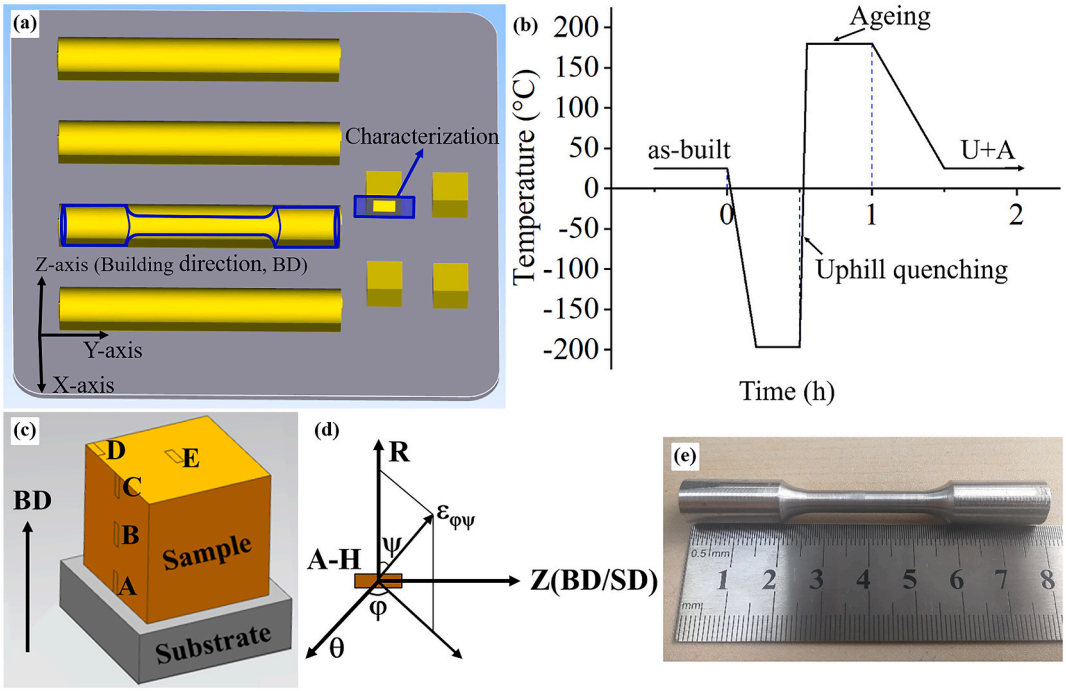

Fig. 1. (a) Schematic illustration of SLMed samples, (b) temperature versus time diagram of the U + A process, (c) schematic showing the measured positions (A ~ E) of each sample used for residual stress measurements, (d) schematic of stress measurement using XRD, and (e) photograph of the tensile specimens after machining.

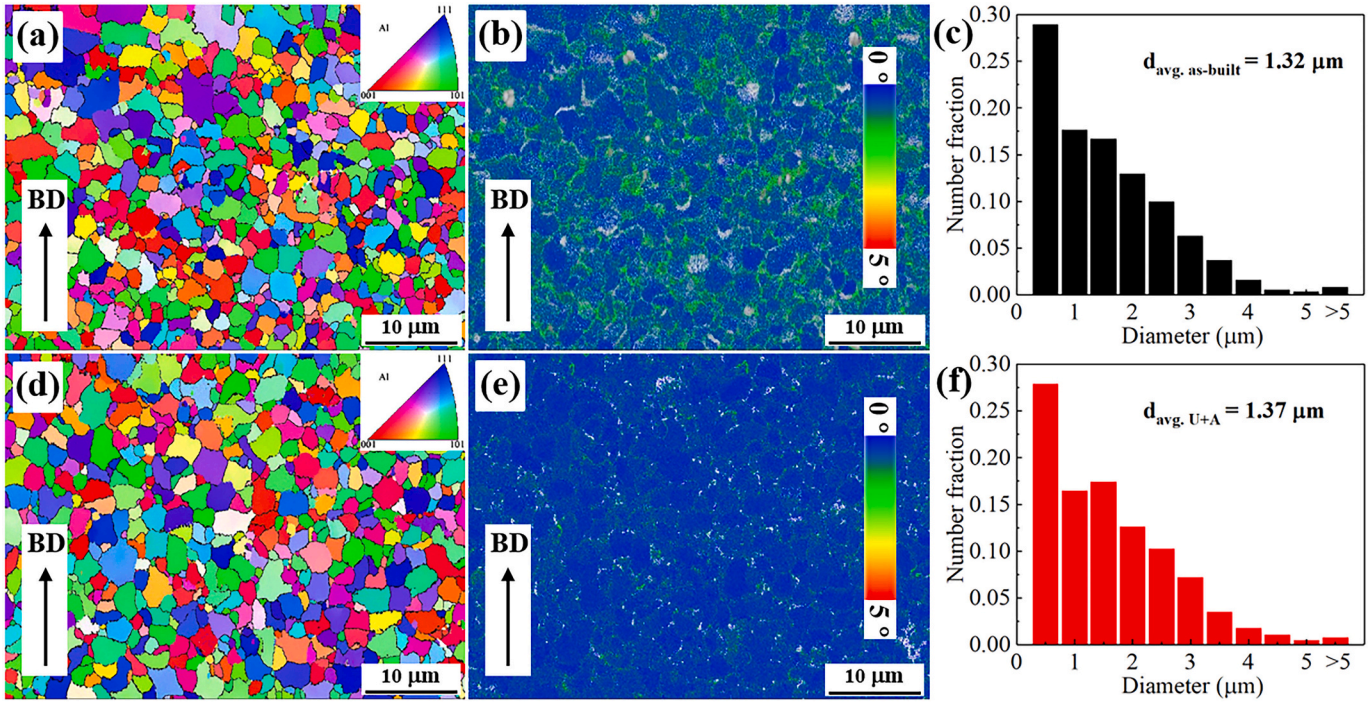

Fig. 2. EBSD results of the SLMed TiB_2/Al-7Si-Mg alloy under as-built condition (a, b, c) and U + A treated condition: (a, d) inverse pole figure (IPF) maps, (b, e) the corresponding kernel average misorientation (KAM) maps, (c, f) the corresponding grain size distribution statistics.

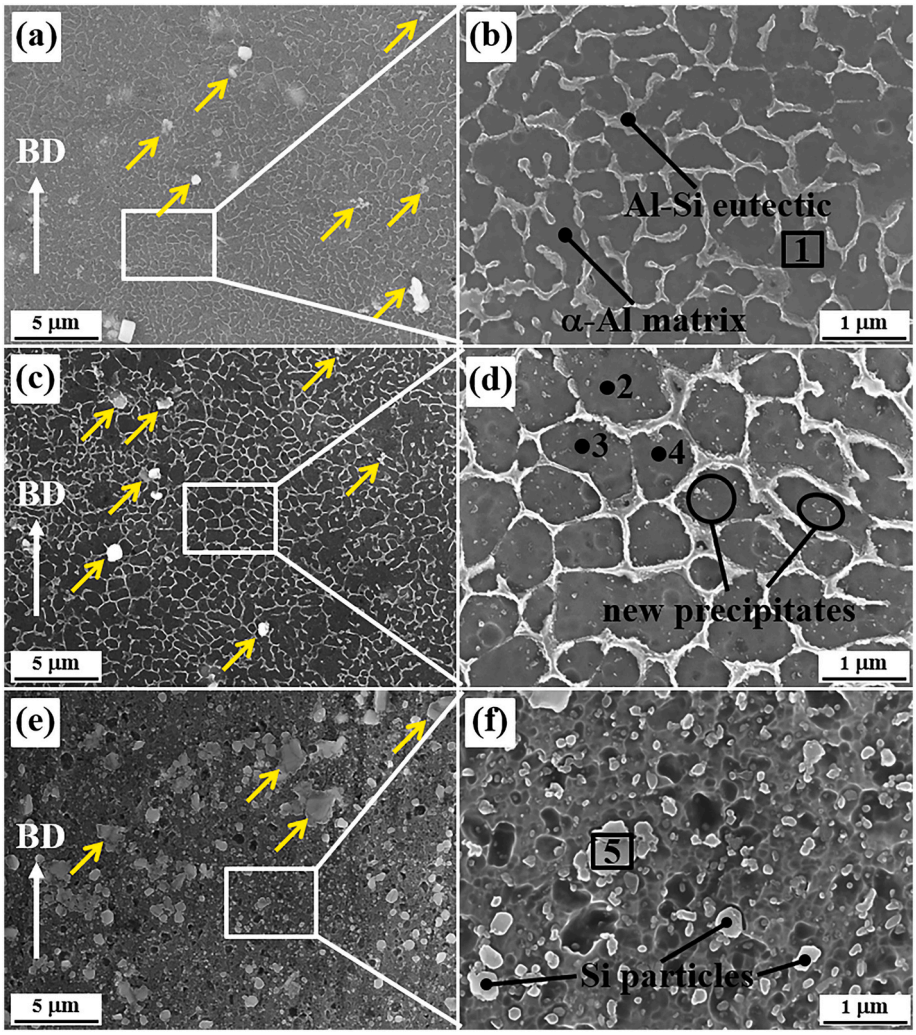

Fig. 3. SEM images of the SLMed TiB_2/Al-7Si-Mg alloy under different treated conditions: (a, b) as-built condition, (c, d) U + A treated condition, (e, f) annealed condition. Yellow arrows in (a, c, e) indicate the nano-TiB_2 particles. (For interpretation of the references to colour in this figure legend, the reader is referred to the web version of this article.)

to the as-built residual stress) and dislocation recovery. In this paper, we applied this approach to an in-situ nano-TiB_2 decorated Al alloy fabricated by SLM [28–30]. The mechanisms for explaining residual stress reduction and strength enhancement are elucidated with the aid of X-ray diffraction (XRD), scanning electron microscopy (SEM), transmission electron microscopy (TEM), and electron backscatter diffraction (EBSD).

2. Experimental procedure

2.1. Materials

In the present study, we used a home-made in-situ nano-TiB_2 decorated Al-7Si-Mg (TiB_2/Al-7Si-Mg) alloy powder, fabricated by the salt-metal reaction and gas atomization, because in-situ TiB_2 particles have various advantages as a reinforcer of Al alloys (details can be found in our previous studies [30–33]). The alloy powders are spherical in shape and have a particle size in the range of 15–53 μm. The chemical compositions of the alloy powder and SLMed sample were determined by Inductively Coupled Plasma Atomic Emission Spectroscopy (ICP-AES; iCAP6300), as presented in Table 1. It can be seen that the proportions of the main alloy elements (Si and Mg) in the SLMed bulk samples are almost the same as those in the initial powders. Besides, the content of nano-TiB_2 particles is approximately 2.47 wt% and it remains stable during the SLM process. Before the SLM process, the alloy powders were dried in a furnace oven at 70 °C for 24 h.

2.2. SLM process and post treatment

The SLM process was carried out on a Prox DMP 200 SLM machine (3D Systems, USA). The 10 × 10 × 10 mm^3 cubic samples for residual stress measurement and microstructure characterization and 80 × 10 × 10 mm^3 cubic samples for tensile testing (Fig. 1a) were produced using the optimal processing parameters based on a series of preliminary tests: laser power of 280 W, scanning speed of 1200 mm/s, layer thickness of 30 μm, hatching space of 100 μm, and scanning strategy of rotation for 90° between layers.

After fabrication, the specimens were cut together with the substrate using a wire-cut electric discharge machine, as presented in Fig. 2c.

Table 2
Local chemical compositions (wt%) of rectangular regions of 1 and 5, and Points 2 to 4 shown in Fig. 3.

Number	Si	Mg
1	3.95	0.46
2	2.31	0.10
3	2.44	0.13
4	2.12	0.08
5	57.3	–

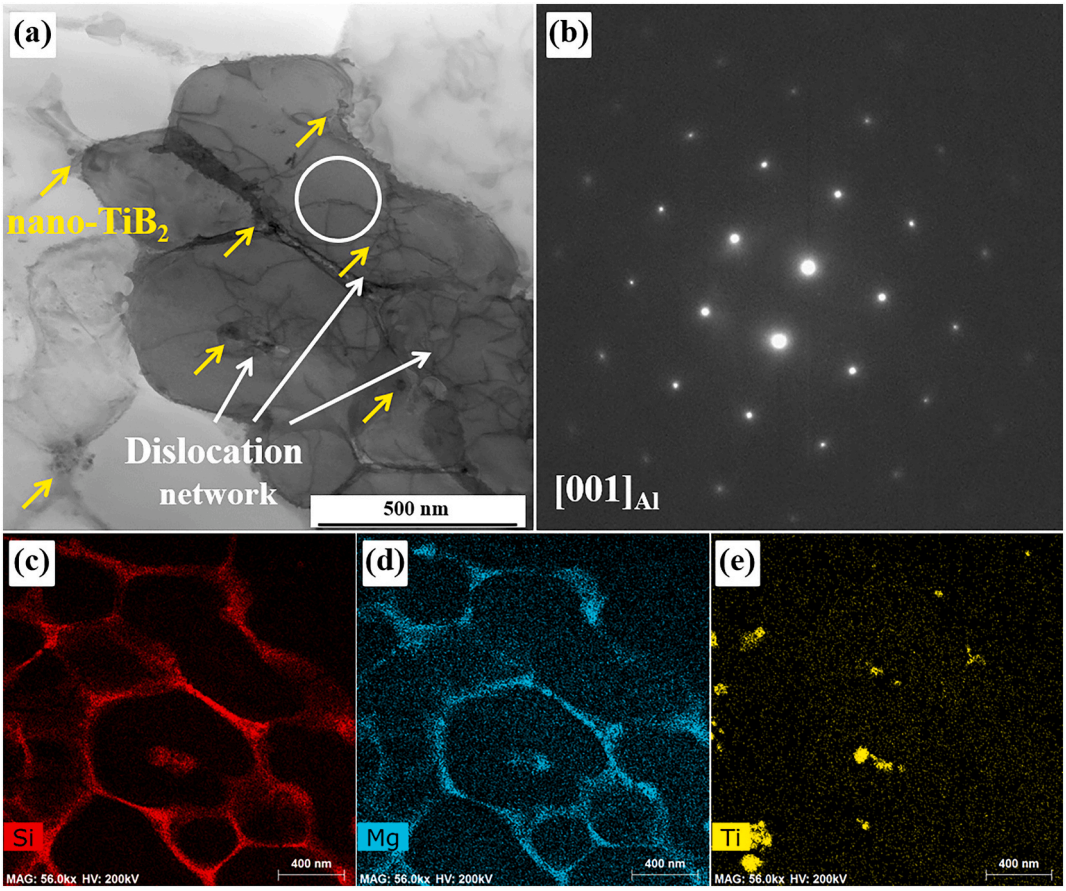

Fig. 4. TEM images of the as-built TiB_2/Al-7Si-Mg alloy: (a) TEM-BF image, (b) corresponding SAED pattern inside the cell (white circle area in (a)), (c-e) the corresponding EDS mappings of Si, Mg and Ti elements. Yellow arrows in (a) indicate the nano-TiB_2 particles. (For interpretation of the references to colour in this figure legend, the reader is referred to the web version of this article.)

Then, the specimens were subjected to the proposed U + A process (Fig. 1b). The as-built samples were first cooled in liquid nitrogen (LN2) at approximately −196 °C for 30 min, followed by an ageing treatment of rapid heating in an oil bath at 180 °C and holding for 30 min. For further investigation, the as-built samples were also U + A processed with different ageing times and temperatures. For comparison, some samples were directly underwent traditional annealed treatment at 300 °C or 500 °C for 2 h [26,27].

2.3. Microstructure characterizations

Microstructure characterizations were performed on the side view of the cubic samples, as presented in Fig. 1a. SEM specimens were firstly grinded to 2500# sandpaper, polished with a 0.5 μm polishing paste, and then etched using Keller's regent (1 vol% HF, 1.5 vol% HCl, 2.5 vol% HNO_3, 95 vol% H_2O) for 60 s. The microstructures were characterized using a scanning electron microscope (SEM, TESCAN MAIA3). Electron backscatter diffraction (EBSD) samples were mechanically ground and ion polished using a Leica EM TIC 3× machine. Then, the samples were characterized using a TESCAN MAIA3 SEM instrument equipped with a BRUKER e-Flash^{HR} EBSD detector at a step size of 70 nm. TEM thin samples were prepared by mechanical polishing and ion thinning using a Precision Ion Polishing System (Gatan Model 691). Then, the samples were examined using an FEI Talos F200X microscope operated at 200 kV and an FEI Titan Themis 300 microscope equipped with a probe aberration corrector and a highly efficient energy dispersive X-ray system at 200 kV for atomic and nano-scale characterization in the scanning TEM (STEM) mode.

2.4. Residual stress

The residual stresses consisting of two components, along the building direction (BD) or scanning direction (SD) and normal to the BD or SD, were evaluated using the PROTO-iXRD X-ray stress analyser with Cr-K_α radiation. To accurately measure the residual stress in the SLMed samples, the samples were pre-treated by mechanical polishing and chemical etching, as proposed in [34]. Al (311) diffraction peaks were chosen for residual stress measurement using the $\sin^2\psi$ method (Fig. 1d). The measured positions on the lateral and top surfaces of the cubic samples are shown in Fig. 1c (labelled A ~ E).

2.5. Mechanical properties

According to the ASTM-E8M standard, the tensile testing specimens were machined (Fig. 1e) and then tested on a Zwick/Roell Z100 machine at room temperature at a constant strain rate of 1×10^{-4} s^{-1}. For each treatment condition, at least three specimens were used.

3. Results and discussion

3.1. Microstructure characterization

The EBSD results of longitudinal-section along the building direction (BD) of the SLMed TiB_2/Al-7Si-Mg alloy under as-built and U + A treated conditions are presented in Fig. 2. From the inverse pole figure (IPF) map in Fig. 2a, it can be seen that the as-built alloy exhibited equiaxed grain structures due to the heterogeneous nucleation effect of nano-TiB_2 particles (detailed explanation can be found in our previous study

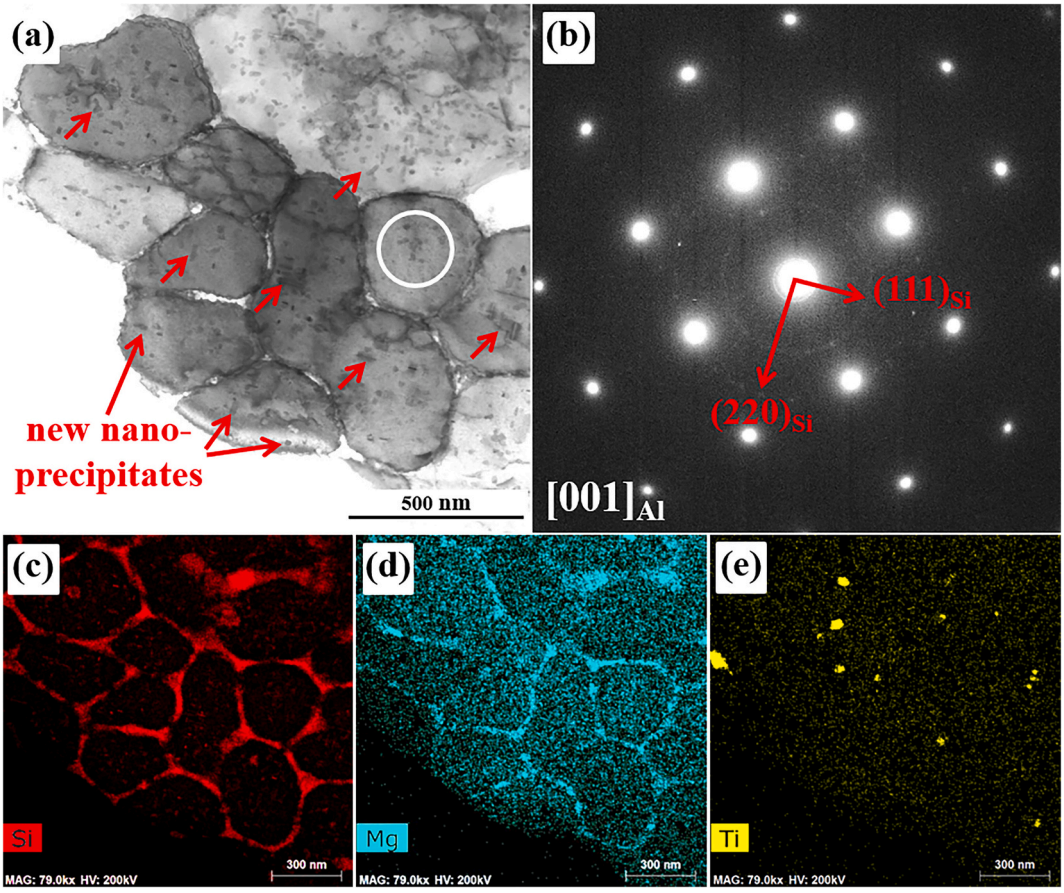

Fig. 5. TEM images of the U + A treated TiB_2/Al-7Si-Mg alloy: (a) TEM-BF image, (b) corresponding SAED pattern inside the cell (white circle area in (a)), (c-e) the corresponding EDS mappings of Si, Mg and Ti elements. Red arrows in (a) indicate the new nano-precipitates. (For interpretation of the references to colour in this figure legend, the reader is referred to the web version of this article.)

[29,30,33]). The corresponding grain size distribution statistic of as-built alloy in Fig. 2c shows that there are more than 46% of grains with a size smaller than 1 μm (ultra-fine grains), and the average grain size is around 1.32 μm. Besides, the corresponding kernel average misorientation (KAM) map in Fig. 2b presents large local misorientations at/near these boundaries, indicating the intense dislocation at eutectic Si cell boundaries. According to our previous studies [33], the stored dislocation density can be as high as 1.74×10^{14} m^{-2} due to the high gradient thermal stress of cycle heating in the SLM process. After U + A treatment, the microstructural features at the grain level remain almost unchanged as shown in Fig. 2d. Fig. 2f presents the average grain size negligible growth to 1.37 μm. It is noteworthy that, in the U + A treated sample, the high dislocation density decreased evidently, as shown in Fig. 2e. The disentanglement of dislocation networks and decrease in dislocation density could be attributed to recovery during the post U + A treatment.

Fig. 3 presents the low magnification (a, c, e) and high magnification (b, d, f) SEM images featuring microstructures of the as-built (a, b), U + A treated (c, d) and annealed alloy TiB_2/Al-7Si-Mg alloy. The corresponding results of local chemical compositions of rectangular regions of 1 and 5, and Points 2 to 4 marked in Fig. 3 using EDS analysis are presented in Table 2. In the as-built alloy (Fig. 3a and b), very fine equiaxed cell-like substructures are formed as a result of fast solidification during the SLM process. It can be seen that the primary α-Al matrix is surrounded by the cellular eutectic Si phase. The mean diameter of cells is approximately 500 nm. Besides, the nano-TiB_2 particles indicated by yellow arrows in Fig. 3a are generally uniformly distributed in the alloy. The EDS analysis at rectangular regions of 1 (Table 2) reveals the super solute of the main elements of Si and Mg in the Al matrix.

After U + A treatment, as shown in Fig. 3c and d, the microstructure consisting of α-Al cells and eutectic Si boundaries remains unchanged. This suggests that the U + A treatment can not destroy the cellular eutectic Si sub-structures formed during rapid solidification. In addition, many new fine precipitates in spherical or short rod-like can be observed inside the α-Al cells, as indicated by black circles in Fig. 3d. The EDS analysis at Points 2 to 4 shows that little Si and Mg are still in solution. Most of Si and Mg are dissipated to form the new precipitates. For comparison, in the alloy after traditional annealed treatment (Fig. 3e and f), the SEM results show that the fine cell microstructures are destroyed. The high temperature during annealing leads to the coarsening of the Si phase. The diameter of relatively coarsened Si particles can reach several micrometers.

Fig. 4 presents the TEM images that exhibit the microstructures of the as-built TiB_2/Al-7Si-Mg alloy. The bright-field (BF) image (Fig. 4a) shows the clear cell structure. The obvious variation of diffraction contrast indicates the large orientation deviation between the neighboring structures, namely grain boundaries. Besides, the results are consistent with the above diameter sizes of grain and cell in EBSD and SEM images, respectively. Thus, it revealed that there are several cell substructures inside one grain. The corresponding EDS mappings in Fig. 4c-e present that Si and Mg atoms segregate along the cell boundaries. Moreover, the majority of nano-TiB_2 particles (yellow arrows in Fig. 4a) are uniformly distributed in the alloy, although some particles tend to distribute along the cell boundaries. In addition, it can be clearly seen that some entangled dislocations inside the cells, as indicated in Fig. 4a. The dislocations interact with each other, with nano-TiB_2 particles and particularly with the cell boundaries. The intense tangled dislocation is consistent with the above KAM results. Besides, as shown

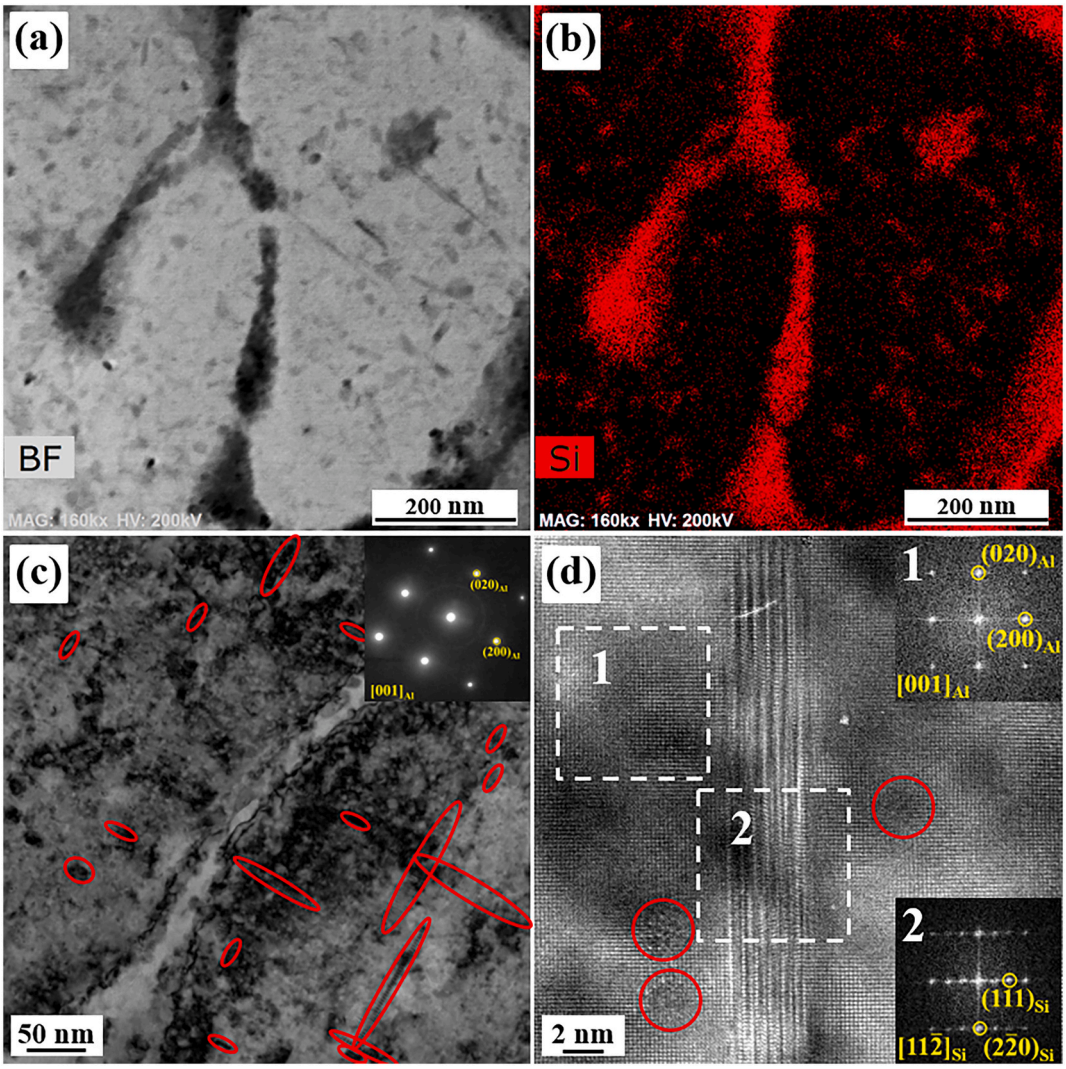

Fig. 6. TEM images of the U + A treated TiB_2/Al-7Si-Mg alloy: (a, c) TEM-BF image, (b) corresponding EDS mappings of Si element of (a), (d) HRTEM of precipitates in (c). Inset in (c) is the corresponding SAED image. Insets in (d) are the corresponding FFT images of white square areas in (d). Red circles in (c, d) indicate the new nano-precipitates. (For interpretation of the references to colour in this figure legend, the reader is referred to the web version of this article.)

in Fig. 4b, the corresponding selected area electron diffraction (SAED) pattern of white circled area inside the cell in Fig. 4a reveals that there are only diffraction spots of Al matrix and no extra reflection spots showing crystallization that corresponded to Si or Mg_xSi_y phase.

Figs. 5 and 6 present the TEM images of TiB_2/Al-7Si-Mg alloy after U + A treatment. As shown in the BF image (Fig. 5a), the ultrafine eutectic Si cellular structures remained after U + A treatment. The corresponding EDS mappings in Fig. 5c-e give that Si and Mg atoms are still segregated along the cell boundaries. In addition, the intense tangled dislocation density decreased after U + A treatment, as shown in Fig. 5a. The disentanglement of dislocation networks and decrease in dislocation density could be attributed to annihilation by recovery during treatment. Meanwhile, as shown in Fig. 5a and Fig. 6a, many new nano-sized precipitates can be observed inside the cell structure, as indicated by the red arrows. The morphology of the precipitates is dot-like or needle-like. As shown in Fig. 5b, the corresponding SAED image of the white circled area in Fig. 5a revealed that the new nano-precipitates are Si particles with a diamond cubic crystal structure. Fig. 6a and c gives the higher magnification BF images and the details of the precipitates can be observed. The precipitates can be identified to be pure Si particles from the elemental mapping in Fig. 6b. Besides, the acicular precipitates have a length of tens of nanometers, and a width of several nanometers. Moreover, as shown in Fig. 6c (in $[001]_{Al}$ zone axes), these elongated precipitates appear with a large aspect ratio in $[100]_{Al}$ zone axes. Thus, the acicular precipitates are aligned parallel or perpendicular to each other. A representative high-resolution TEM (HRTEM) micrograph along with the FFT images for the needle-like precipitate is presented in Fig. 6d. The results of HRTEM confirm the diamond cubic crystal structure of Si precipitates. The orientation relationship between the Al matrix and needle-like precipitate is determined as $\langle 001\rangle_{Al}//<11\bar{2}>_{Si}$ and $\{200\}_{Al}//\{111\}_{Si}$. Besides, the Si particles were highly faulty with stacking faults and dislocations, which compensated the lattice misfit between the Al (200) and Si (111) planes. Therefore, the interface between the Si needles and the Al matrix was semi-coherent. In addition, it is noteworthy that some finer spherical precipitates (around 2 nm) are visible in the HRTEM image. However, these precipitates do not exhibit a clear atomic arrangement and can not be distinguished using the FFT image.

3.2. Residual stress development

Fig. 7a shows the experimental results for residual stress at points A ~ E points in the as-built and U + A treated TiB_2/Al-7Si-Mg alloy. In line with other studies [19,21], very high residual stress (up to approximately 50% of yielding stress) was observed in the as-built sample. At

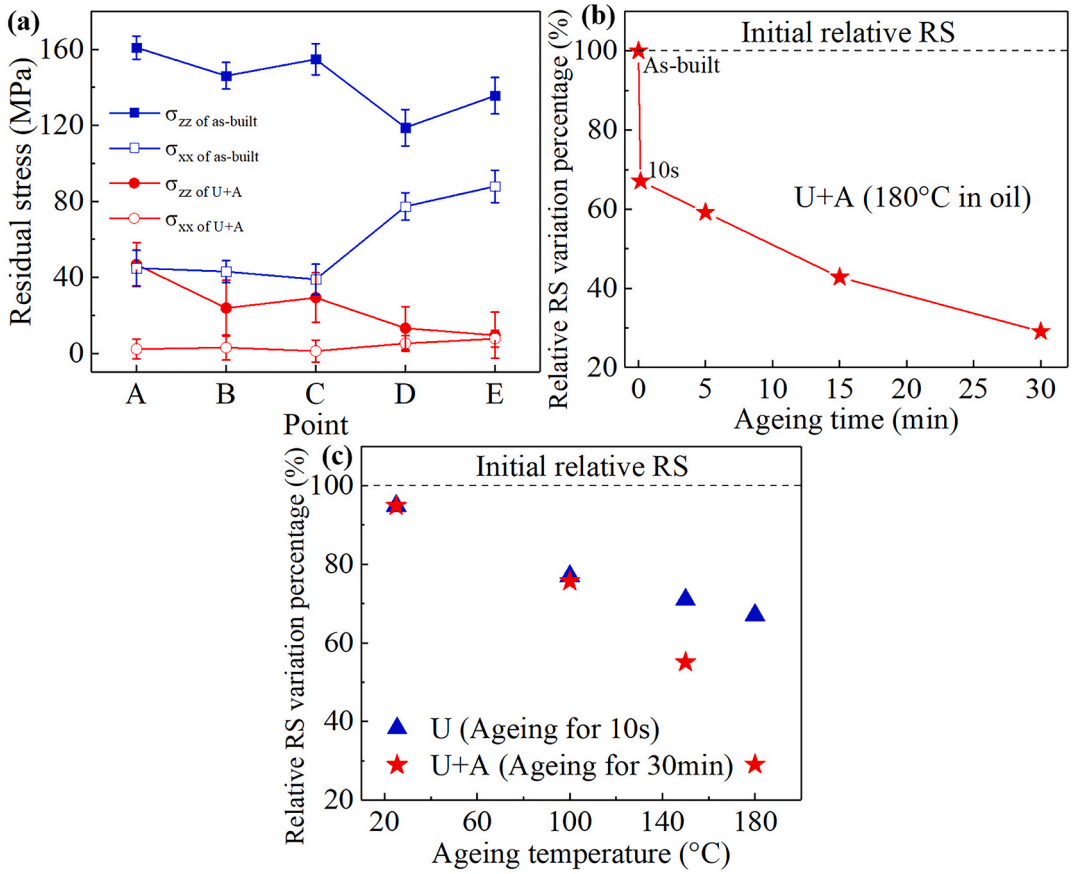

Fig. 7. Development of residual stress (RS) ($\sigma_{BD/SD}$ and $\sigma_{\perp BD/SD}$) at points A ~ E of as-built and U + A treated samples. (b) residual stress (σ_{BD}) development with ageing time at point A during the U + A process and (c) residual stress (σ_{BD}) development at the different ageing temperatures at point A.

Table 3
Residual stress (σ_{BD}) development at point An under different treatment conditions.

Label	Treatment process	Relative residual stress variation percentage (%)
A1	180 °C/30 min in air furnace	57
B1	300 °C/2 h	17
B2	500 °C/2 h	~0
B3	500 °C/2 h + U (180 °C/10 s)	−32

the lateral surface, the stress values along the BD (σ_{BD}) were higher than those normal to the BD ($\sigma_{\perp BD}$). With increasing distance from the substrate to the top of the samples, the stress values in the middle of the lateral surface decreased first and then increased. Additionally, the highest residual stress along the BD (160.9 MPa) was at the junction between the sample and substrate. At the top surface, stress along the SD (σ_{SD}) was higher than that normal to the SD ($\sigma_{\perp SD}$), and the highest residual stress occurred in the middle of the top surface. After U + A treatment, the residual stress was efficiently relieved in both directions. The average residual stresses in the two directions were reduced to only 20.9 MPa ($\sigma_{BD/SD}$) and 3.8 MPa ($\sigma_{\perp BD/SD}$). The highest residual stress was reduced to an acceptable level of 29.3 MPa.

To understand the residual stress evolution during the U + A treatment, we set the initial maximum residual stress (σ_{BD}) at point A 100% and then investigated the relative residual stress variation under different treatment conditions. The U + A process can be divided into two stages: up-quenching and ageing. Fig. 7b shows the evolution of residual stress as a function of ageing time (at 180 °C) after up-quenching. The residual stress decreased significantly (approximately 33%) after up-quenching in oil at 180 °C without ageing (this sample was taken out within 10 s). Then, in the following ageing stage, the residual stress decreased gradually with ageing time, finally by 71% after U + A for 30 min. The above results indicate that both up-quenching and ageing are responsible for the reduction of residual stress in the SLMed samples. To elucidate the contribution of the ageing treatment to residual stress relaxation, the sample was directly aged at 180 °C for 30 min in an air furnace (A1), and the residual stress was decreased by 43% (as shown in Table 3). Additionally, when the sample was annealed at 300 °C for 2 h (B1), the residual stress was relaxed significantly by nearly 83%. Annealing at 500 °C for 2 h (B2) fully reduced the residual stress to 0. Furthermore, the fully annealed sample (500 °C/2 h) was subjected to the uphill quenching process and then immediately removed (B3). Reverse compressive stresses were detected in the samples, and this result shows that up-quenching can introduce compressive stress on the surface layer of the samples.

The effects of up-quenching and ageing on residual stress relaxation are discussed in the following. In the up-quenching stage after the cryogenic treatment, the exterior regions (in contact with the oil) were heated violently by the oil (from −196 °C to 180 °C, $\Delta T = 376$ °C), while the interior remained at a low temperature. Thus, the exterior regions expanded faster than the interior, resulting in a new distribution of misfit strain. The strain in the exterior can be estimated as:

$$\varepsilon = \alpha_l \times \Delta T \quad (1)$$

If we take the coefficient of thermal expansion α_l to be 2×10^{-5} /°C, we get $\varepsilon = 7.52 \times 10^{-3}$. This thermal strain is much higher than the yielding strain of the material (2×10^{-3}). Thus, plastic deformation is expected in the exterior regions. Therefore, the uphill quenching process

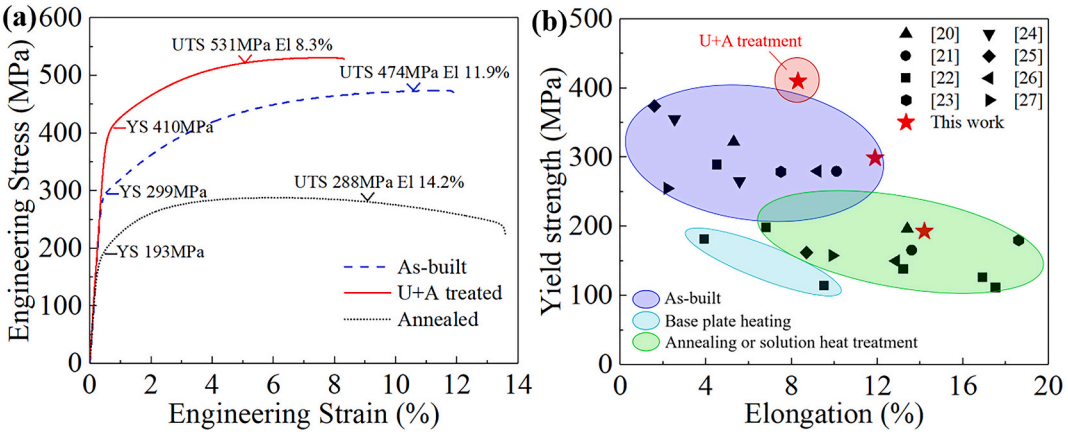

Fig. 8. (a) Typical tensile stress-strain curves of as-built, U + A treated, and annealed TiB_2/Al samples. The corresponding YS, UTS, and El under different conditions are marked on the curves. (b) A summary of YS versus El of SLMed Al—Si alloys under different conditions (base plate heating, annealing, and solution heat treatment) for relaxation of residual stress.

can produce compressive stresses on the surface layer of the SLMed samples, which offsets the initial SLMed tensile residual stresses. As can be seen in Fig. 7c, when we changed the final ageing treatment temperature from 180 °C to lower temperatures (150 °C, 100 °C, and 25 °C), the reduction in residual stress decreased with decreasing of ageing temperature (ΔT decreased).

Furthermore, during the following ageing stage, the thermal relaxation of residual stress (recovery) at 180 °C in the oil bath also plays an important role in residual stress reduction. This residual stress relaxation is controlled by thermally activated processes and can be described by the Zener-Wert-Avrami function [35]:

$$\frac{\sigma^{RS}}{\sigma_0^{RS}} = exp[-(At)^m] \tag{2}$$

$$A = Bexp\left[\frac{-Q}{RT}\right] \tag{3}$$

where σ^{RS} is the varying residual stress, σ_0^{RS} is the initial residual stress, m is a parameter depending on the dominant relaxation mechanism, t is the ageing time, B is a constant, Q is the activation enthalpy for the relaxation of residual stress, k is the Boltzmann constant, and T is the ageing temperature. Ageing at 180 °C released residual stress effectively in this study, as shown in Fig. 7. Our results are consistent with Refs. [36, 37] in that residual stress can be partially relaxed at temperatures of 150 °C and 175 °C. The KAM maps in Fig. 2 and TEM results in Figs. 4 and 5 show the intense dislocation at eutectic Si cell boundaries and inside the cells in the as-built sample. While after U + A treatment, the dislocation density decreased obviously. And we attribute the disentanglement of dislocation networks and decrease in dislocation density to recovery, which significantly reduces the residual stress. The stored dislocations can be as high as 1.74×10^{14} m^{-2} in SLMed Al alloy, which provides a large driving force for recovery. During recovery, the relaxation of residual stress might be closely related to the release of the stored high energy formed during SLM processing. In other words, residual stress is partly counteracted by the newly produced residual stress, which is opposite to the original residual stress and partly reduced by recovery.

3.3. Mechanical properties

The U + A treatment also led to an increase in strength. The tensile stress-strain curves of the as-built and post-treated samples as well as the corresponding yield strength (YS), ultimate tensile strength (UTS), and elongation (El) are shown in Fig. 8a. After the U + A treatment, YS increased by 37% from 299 MPa to 410 MPa and UTS increased by 12% from 474 MPa to 531 MPa. For the samples annealed at 300 °C for 2 h, which is the method commonly used to reduce residual stress, YS and UTS decreased to approximately 193 MPa and 288 MPa, respectively. Fig. 8b summarizes the values of strength and ductility for SLMed Al—Si alloys reported in the literature under different conditions [20–27]. Consistent with our results, previous studies concluded that the SLM process results in the presence of a large residual stress in as-built samples. In these studies, in-situ base plate heating, post annealing, or solution heat treatment were applied to release the residual stress. However, these methods significantly decrease the strength, whereas the proposed U + A treatment can increase the strength and reduce residual stress simultaneously.

The advantage of the proposed U + A treatment is that the process barely changes the hierarchical microstructure, including grains and cell structures, in SLMed samples. From the EBSD results in Fig. 2, we revealed that the microstructural features at the grain level remain unchanged. From the SEM results in Fig. 3, the ultrafine eutectic Si cellular structures remained after U + A treatment. The unchanged grain and cell boundaries can still impede the dislocation motion, contributing to high strength. Meanwhile, from the TEM results, the new nano-Si particles precipitate inside the cells. These nanosized Si particles formed during U + A treatment could contribute to precipitation strengthening. Although the Si and Mg in solution decrease, and thus the contribution to strength by the solid solution strengthening decreases. Besides, the dislocation density decreases during the treatment, as mentioned above, and thus the contribution to strength by dislocation density strengthening decreases. Finally, we speculate that the reduction by solid solution strengthening and dislocation density strengthening can be counterbalanced by the increment of precipitation strengthening. However, during the traditional annealed treatment at high temperatures, the fine Si cellular structures collapse and break into large Si particles, which is the reason for the strength reduction.

4. Conclusions

In conclusion, U + A processing has been demonstrated as an effective approach to reduce residual stress while improve the strength of SLMed TiB_2/Al-7Si-Mg samples. After U + A treatment, the highest residual stress was reduced to an acceptable level (<30 MPa) because of the newly produced stress opposite to the original stress and recovery of dislocations. Meanwhile, the samples exhibited a higher yield strength of 410 MPa, ultimate tensile strength of 531 MPa, and reliable elongation of 8.3%. The desired microstructures, such as ultra-fine grains and cells, persist after the U + A treatment. While substantial new nano-Si particles with dot-like or needle-like morphology precipitate inside the

cells. The enhanced strength is mainly due to precipitation strengthening by dispersed nanosized Si precipitates. The proposed U + A strategy is expected to be useful in other materials and components fabricated by SLM in which residual stress is also unwanted.

Declaration of Competing Interest

The authors declare that they have no known competing financial interests or personal relationships that could have appeared to influence the work reported in this paper.

Acknowledgements

This work was financially supported by the National Key Research and Development Program of China (Grant No. 2016YFB1100100) and the Natural Science Foundation of China (Grant No. 51971137). The authors thank TESCAN China for EBSD characterizations.

References

[1] D. Herzog, V. Seyda, E. Wycisk, C. Emmelmann, Additive manufacturing of metals, Acta Mater. 117 (2016) 371–392, https://doi.org/10.1016/j.actamat.2016.07.019.
[2] B.H. Jared, M.A. Aguilo, L.L. Beghini, B.L. Boyce, B.W. Clark, A. Cook, B.J. Kaehr, J. Robbins, Additive manufacturing: toward holistic design, Scr. Mater. 135 (2017) 141–147, https://doi.org/10.1016/j.scriptamat.2017.02.029.
[3] N. Shamsaei, A. Yadollahi, L. Bian, S.M. Thompson, An overview of direct laser deposition for additive manufacturing; part II: mechanical behavior, process parameter optimization and control, Additive Manufacturing. 8 (2015) 12–35, https://doi.org/10.1016/j.addma.2015.07.002.
[4] Y. Morris Wang, T. Voisin, J.T. McKeown, J. Ye, N.P. Calta, Z. Li, Z. Zeng, Y. Zhang, W. Chen, T.T. Roehling, R.T. Ott, M.K. Santala, P.J. Depond, M.J. Matthews, A. V. Hamza, T. Zhu, Additively manufactured hierarchical stainless steels with high strength and ductility, Nat. Mater. 17 (2017) 63–71, https://doi.org/10.1038/nmat5021.
[5] T. DebRoy, H.L. Wei, J.S. Zuback, T. Mukherjee, J.W. Elmer, J.O. Milewski, A. M. Beese, A. Wilson-Heid, A. De, W. Zhang, Additive manufacturing of metallic components – process, structure and properties, Prog. Mater. Sci. 92 (2018) 112–224, https://doi.org/10.1016/j.pmatsci.2017.10.001.
[6] J.L. Bartlett, X. Li, An overview of residual stresses in metal powder bed fusion, Additive Manufacturing. 27 (2019) 131–149.
[7] D.D. Gu, W. Meiners, K. Wissenbach, R. Poprawe, Laser additive manufacturing of metallic components: materials, processes and mechanisms, Int. Mater. Rev. 57 (2012) 133–164, https://doi.org/10.1179/1743280411Y.0000000014.
[8] A. Salmi, E. Atzeni, History of residual stresses during the production phases of AlSi10Mg parts processed by powder bed additive manufacturing technology, Virtual and Physical Prototyping. 12 (2017) 153–160, https://doi.org/10.1080/17452759.2017.1310439.
[9] L. Wang, X. Jiang, Y. Zhu, X. Zhu, J. Sun, B. Yan, An approach to predict the residual stress and distortion during the selective laser melting of AlSi10Mg parts, Int. J. Adv. Manuf. Technol. 97 (2018) 3535–3546, https://doi.org/10.1007/s00170-018-2207-3.
[10] L.M. Sochalski-Kolbus, E.A. Payzant, P.A. Cornwell, T.R. Watkins, S.S. Babu, R. R. Dehoff, M. Lorenz, O. Ovchinnikova, C. Duty, Comparison of residual stresses in Inconel 718 simple parts made by Electron beam melting and direct laser metal sintering, Metall and Mat Trans A. 46 (2015) 1419–1432, https://doi.org/10.1007/s11661-014-2722-2.
[11] A.J. Dunbar, E.R. Denlinger, J. Heigel, P. Michaleris, P. Guerrier, R. Martukanitz, T. W. Simpson, Development of experimental method for in situ distortion and temperature measurements during the laser powder bed fusion additive manufacturing process, Additive Manufacturing. 12 (2016) 25–30, https://doi.org/10.1016/j.addma.2016.04.007.
[12] X. Zhao, A. Iyer, P. Promoppatum, S.-C. Yao, Numerical modeling of the thermal behavior and residual stress in the direct metal laser sintering process of titanium alloy products, Additive Manufacturing. 14 (2017) 126–136, https://doi.org/10.1016/j.addma.2016.10.005.
[13] J. Song, W. Wu, L. Zhang, B. He, L. Lu, X. Ni, Q. Long, G. Zhu, Role of scanning strategy on residual stress distribution in Ti-6Al-4V alloy prepared by selective laser melting, Optik. 170 (2018) 342–352, https://doi.org/10.1016/j.ijleo.2018.05.128.
[14] P. Mercelis, J. Kruth, Residual stresses in selective laser sintering and selective laser melting, Rapid Prototyp. J. 12 (2006) 254–265, https://doi.org/10.1108/13552540610707013.
[15] T. Simson, A. Emmel, A. Dwars, J. Böhm, Residual stress measurements on AISI 316L samples manufactured by selective laser melting, Additive Manufacturing. 17 (2017) 183–189, https://doi.org/10.1016/j.addma.2017.07.007.
[16] B. Vrancken, V. Cain, R. Knutsen, J. Van Humbeeck, Residual stress via the contour method in compact tension specimens produced via selective laser melting, Scr. Mater. 87 (2014) 29–32, https://doi.org/10.1016/j.scriptamat.2014.05.016.
[17] E.R. Denlinger, M. Gouge, J. Irwin, P. Michaleris, Thermomechanical model development and in situ experimental validation of the laser powder-bed fusion process, Additive Manufacturing. 16 (2017) 73–80, https://doi.org/10.1016/j.addma.2017.05.001.
[18] M. Shiomi, K. Osakada, K. Nakamura, T. Yamashita, F. Abe, Residual stress within metallic model made by selective laser melting process, CIRP Ann. 53 (2004) 195–198, https://doi.org/10.1016/S0007-8506(07)60677-5.
[19] X.P. Li, X.J. Wang, M. Saunders, A. Suvorova, L.C. Zhang, Y.J. Liu, M.H. Fang, Z. H. Huang, T.B. Sercombe, A selective laser melting and solution heat treatment refined Al–12Si alloy with a controllable ultrafine eutectic microstructure and 25% tensile ductility, Acta Mater. 95 (2015) 74–82, https://doi.org/10.1016/j.actamat.2015.05.017.
[20] W. Li, S. Li, J. Liu, A. Zhang, Y. Zhou, Q. Wei, C. Yan, Y. Shi, Effect of heat treatment on AlSi10Mg alloy fabricated by selective laser melting: microstructure evolution, mechanical properties and fracture mechanism, Mater. Sci. Eng. A 663 (2016) 116–125, https://doi.org/10.1016/j.msea.2016.03.088.
[21] J.H. Rao, Y. Zhang, X. Fang, Y. Chen, X. Wu, C.H.J. Davies, The origins for tensile properties of selective laser melted aluminium alloy A357, Additive Manufacturing. 17 (2017) 113–122, https://doi.org/10.1016/j.addma.2017.08.007.
[22] K.G. Prashanth, S. Scudino, J. Eckert, Defining the tensile properties of Al-12Si parts produced by selective laser melting, Acta Mater. 126 (2017) 25–35, https://doi.org/10.1016/j.actamat.2016.12.044.
[23] N. Takata, H. Kodaira, K. Sekizawa, A. Suzuki, M. Kobashi, Change in microstructure of selectively laser melted AlSi10Mg alloy with heat treatments, Mater. Sci. Eng. A 704 (2017) 218–228, https://doi.org/10.1016/j.msea.2017.08.029.
[24] Y. Bai, Y. Yang, Z. Xiao, M. Zhang, D. Wang, Process optimization and mechanical property evolution of AlSiMg0.75 by selective laser melting, Materials & Design 140 (2018) 257–266, https://doi.org/10.1016/j.matdes.2017.11.045.
[25] P. Ma, K. Prashanth, S. Scudino, Y. Jia, H. Wang, C. Zou, Z. Wei, J. Eckert, Influence of annealing on mechanical properties of Al-20Si processed by selective laser melting, Metals. 4 (2014) 28–36, https://doi.org/10.3390/met4010028.
[26] M. Wang, B. Song, Q. Wei, Y. Zhang, Y. Shi, Effects of annealing on the microstructure and mechanical properties of selective laser melted AlSi7Mg alloy, Mater. Sci. Eng. A 739 (2019) 463–472, https://doi.org/10.1016/j.msea.2018.10.047.
[27] M. Fousová, D. Dvorský, A. Michalcová, D. Vojtěch, Changes in the microstructure and mechanical properties of additively manufactured AlSi10Mg alloy after exposure to elevated temperatures, Mater. Charact. 137 (2018) 119–126, https://doi.org/10.1016/j.matchar.2018.01.028.
[28] M. Chen, X. Li, G. Ji, Y. Wu, Z. Chen, W. Baekelant, K. Vanmeensel, H. Wang, J.-P. Kruth, Novel composite powders with uniform TiB2 Nano-particle distribution for 3D printing, Appl. Sci. 7 (2017) 250, https://doi.org/10.3390/app7030250.
[29] Y. Xiao, Z.Y. Bian, Y. Wu, G. Ji, Y.Q. Li, M.J. Li, Q. Lian, Z. Chen, A. Addad, H. W. Wang, Effect of nano-TiB2 particles on the anisotropy in an AlSi10Mg alloy processed by selective laser melting, J. Alloys Compd. 798 (2019) 644–655, https://doi.org/10.1016/j.jallcom.2019.05.279.
[30] X.P. Li, G. Ji, Z. Chen, A. Addad, Y. Wu, H.W. Wang, J. Vleugels, J. Van Humbeeck, J.P. Kruth, Selective laser melting of nano-TiB2 decorated AlSi10Mg alloy with high fracture strength and ductility, Acta Mater. 129 (2017) 183–193, https://doi.org/10.1016/j.actamat.2017.02.062.
[31] J. Liu, Z. Chen, F. Zhang, G. Ji, M. Wang, Y. Ma, V. Ji, S. Zhong, Y. Wu, H. Wang, Simultaneously increasing strength and ductility of nanoparticles reinforced Al composites via accumulative orthogonal extrusion process, Materials Research Letters. 6 (2018) 406–412, https://doi.org/10.1080/21663831.2018.1471421.
[32] Y. Ma, A. Addad, G. Ji, M.-X. Zhang, W. Lefebvre, Z. Chen, V. Ji, Atomic-scale investigation of the interface precipitation in a TiB2 nanoparticles reinforced Al–Zn–mg–cu matrix composite, Acta Mater. 185 (2020) 287–299, https://doi.org/10.1016/j.actamat.2019.11.068.
[33] Y.K. Xiao, Q. Yang, Z.Y. Bian, H. Chen, Y. Wu, Q. Lian, Z. Chen, H.W. Wang, Microstructure, heat treatment and mechanical properties of TiB2/Al-7Si-cu-mg alloy fabricated by selective laser melting, Mater. Sci. Eng. A 140951 (2021), https://doi.org/10.1016/j.msea.2021.140951.
[34] Y. Chen, H. Sun, Z. Li, Y. Wu, Y. Xiao, Z. Chen, S. Zhong, H. Wang, Strategy of residual stress determination on selective laser melted Al alloy using XRD, Materials. 13 (2020) 451, https://doi.org/10.3390/ma13020451.
[35] M.-C. Berger, J.K. Gregory, Residual stress relaxation in shot peened Timetal 21s, Mater. Sci. Eng. A 263 (1999) 200–204.
[36] B.X. Feng, X.N. Mao, G.J. Yang, L.L. Yu, X.D. Wu, Residual stress field and thermal relaxation behavior of shot-peened TC4-DT titanium alloy, Mater. Sci. Eng. A 512 (2009) 105–108, https://doi.org/10.1016/j.msea.2009.01.028.
[37] H.-J. Lim, D.-H. Ko, D.-C. Ko, B.-M. Kim, Reduction of residual stress and improvement of dimensional accuracy by uphill quenching for Al6061 tube, Metall. Mater. Trans. B 45 (2014) 472–481, https://doi.org/10.1007/s11663-013-9997-3.